Quantitative Precipitation Estimation using X-Band Radar for Orographic Rainfall in the San Francisco Bay Area

Sounak Kumar Biswas, *Student Member, IEEE,* Robert Cifelli, and V. Chandrasekar, *Fellow, IEEE*

***Abstract*—In the San Francisco Bay Area, precipitation occurs in the wintertime, mostly as rain. Wintertime rainfall can be further classified into cold or stratiform rain with a typical radar bright band signature and warm orographic rain with absence of a radar bright band. Vertical Pointing S-Band profiler radar and disdrometer measurements from two of NOAA's Hydrometeorology Testbed (HMT) sites in California are used to study the differences in microphysical properties between these two types of rain and their implications in radar rainfall estimation. A methodology has been developed to discriminate non bright band (NBB) rainfall from bright band (BB) rainfall using reflectivity (Z) and differential reflectivity (Z_{DR}) computed from disdrometer data. Delineating the two rainfall types in this way allowed for an algorithm to be applied to the radar scans to identify rainfall types and apply appropriate reflectivity based and specific differential phase (K_{DP}) based rainfall estimators. Recently, a gap-filling X-Band weather radar with dual-polarization capabilities was deployed in the San Francisco Bay Area in Santa Rosa to aid in weather monitoring and provide high resolution Quantitative Precipitation Estimation (QPE) products. When applied to real radar observations, this method shows great potential for improving the QPE compared to traditional operational products which more often tend to underestimate rainfall in the California coastal region.**

***Index Terms*—X-Band, dual-polarization, reflectivity, differential reflectivity, specific differential phase, bright band, orographic, stratiform.**

I. Introduction

ACCURATE estimation of precipitation is crucial for a variety of practical applications ranging from weather forecasting, flood warning to water resources management. However, oftentimes the measurement accuracy is curtailed by various basic and applied science issues [1]. One such example is precipitation monitoring in regions of complex topography. Remote sensing of precipitation is commonly performed with weather radars, which can be ground based, airborne or space based [1]–[5]. This study focuses on Quantitative Precipitation Estimation (QPE) using a ground based X-Band weather radar over the coastal mountain region of San Francisco Bay Area.

Sounak Kumar Biswas is with the Physical Sciences Laboratory (PSL), National Oceanic and Atmospheric Administration (NOAA)'s Earth System Research Laboratory, Boulder, CO 80305, USA, and also with the Department of Electrical and Computer Engineering, Colorado State University, Fort Collins, CO 80523, USA. (email: sounak.biswas@colostate.edu; sounak.biswas@noaa.gov

Robert Cifelli is with the Physical Sciences Laboratory (PSL), National Oceanic and Atmospheric Administration (NOAA)'s Earth System Research Laboratory, Boulder, CO 80305, USA.

V. Chandrasekar is with the Department of Electrical and Computer Engineering, Colorado State University, Fort Collins, CO 80523, USA.

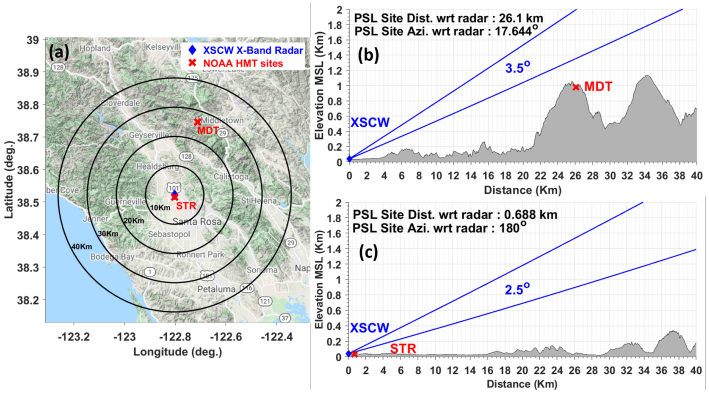

Fig. 1. (a) A map of the northern region of the San Francisco Bay Area, highlighting the domain of the XSCW X-Band radar. The radar is located at Santa Rosa. The black circles represent radar range circles at every 10 km increment. The red crosses represent NOAA Hydro Meteorological Testbed (HMT) ground instrumentation sites, one at Santa Rosa (STR) and the other at Middletown (MDT). Each site contains a S-Band Profiler radar, a Parsivel2 disdrometer and a rain gauge. (b) shows the location of the MDT site relative to the radar along the line of sight azimuth direction along with the radar beam. (c) is same as (b) but for the STR site.

National Weather Service operated S-Band weather radars or WSR-88Ds, in these types of regions, are often associated with inaccurate rainfall estimation due to a number of difficulties posed by the complexity of the terrain. A widespread flooding event at Oroville in Northern California in early 2017 has demonstrated limitations of operational QPE and QPF products where rainfall estimates were greatly underestimated for that event [6], [7]. Several factors, such as radar beam blockage, radar beam overshooting, discontinuity in vertical profile of reflectivity (VPR) and variation in Drop Size Distribution (DSD) limit the accuracy of rainfall measurement. Among these, DSD variability most significantly affects the mean relationships between rainfall and the radar observables. Cool season stratiform or Bright-band (BB) rainfall occurs when precipitation extends well above the freezing level and particles melt as they fall through the melting layer. As the particles melt and develop a liquid water coating on the surface, the radar reflectivity at horizontal polarization is greatly enhanced thus producing a distinct peak in the vertical reflectivity profile, also known as bright band. In contrast, orographic rainfall occurs by warm rain process when rainfall is shallow (below freezing) and enhanced by topography. In mountainous regions, usually, storms are strongly influenced by orographic enhancements which in turn affects the intensity,

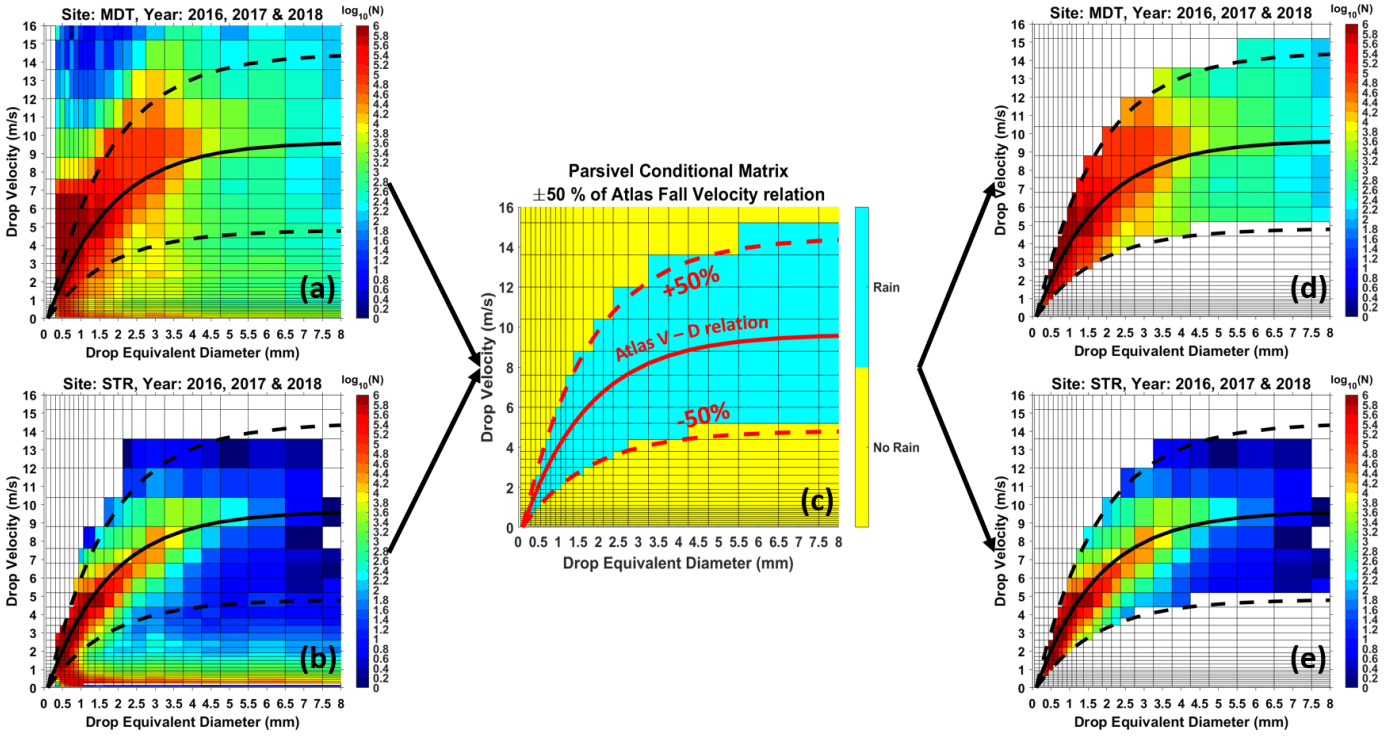

Fig. 2. (a) and (b) shows raw disdrometer observations at MDT and STR sites respectively from year 2016 to 2018 presented as fall velocity vs drop diameter color density plot. The solid black line denotes the ideal Atlas fall velocity vs drop diameter relation. The dashed black lines denote $\pm 50\%$ tolerance lines. (c) represents the Parsivel Conditional Matrix used for quality control purpose. The ideal Atlas fall velocity vs drop diameter relation and $\pm 50\%$ tolerance lines are shown in red. The region shaded in blue is considered as rain. The region outside shaded in yellow denotes no rain. (d) and (e) are quality controlled disdrometer observations at MDT and STR sites respectively. Here, again, the ideal Atlas fall velocity vs drop diameter relation and $\pm 50\%$ tolerance lines are shown in black.

duration, and spatial variability of precipitation. This type of precipitation systems are often shallow, do not exhibit high echo tops and occurs mostly in lower levels of the atmosphere. Therefore, they are more often undersampled by the operational WSR-88D radars in this region due to beam overshooting at distant ranges [8]. Thus, orographic rain is associated with microphysical characteristics which are different from typical stratiform rainfall [9] and all these effects in combination poses a major challenge in radar QPE in complex terrain.

[9] examined S-PROF observations from the strong El Nino winter of 1997-1998 at coastal mountain region near Cazadero in California. They observed that a significant period of rainfall manifested in absence of the radar Bright-band (BB) signature, which is a characteristic of winter stratiform rainfall. The authors pointed out this type of non Bright-band (NBB) rainfall is different from convective rainfall and accompanied with orographic enhancement. Collocated disdrometer observations further revealed that rainfall during this NBB period is associated with greater number of small drops and few large drops compared to BB period. [10] also pointed out this contrasting nature of drop size distribution in NBB rain periods and showed that it yielded an empirical radar rainfall Z-R relation at S-Band which is significantly different from the default ones used by NWS. [11] studied S-PROF data from southeastern USA HMT sites at New Bern and Old Fort during different winters and concluded the presence of NBB rainfall not only in mountainous coastal terrain but also in the relatively flat region where orographic forced rainfall is less likely. [12] also recorded occurrences of NBB rainfall in California's flat central valley. These studies conclusively show presence of NBB rainfall in flat regions surrounding coastal mountains and the need of hybrid radar rainfall relations in order to capture the orographic precipitation accurately.

Traditional radar based QPE approach uses radar reflectivity (Z) for obtaining rainfall rate (R) [13], [14]. For example, the WSR-88D radars use several fixed $Z - R$ relations according to different rainfall categories such as stratiform, convective, tropical and monsoon [15]. Rainfall estimators of this type can be sufficient in areas with a uniform DSD which do not vary much on spatial and temporal scales [16]. Additional utilization of polarimetric radar variables such as differential reflectivity (Z_{DR}) and specific differential phase (K_{DP}) has been found to further enhance radar based QPE [17]. It has been established that K_{DP} is dependent on forward scattering and scales with frequency under Rayleigh scattering assumptions. Furthermore, K_{DP} is found to be less sensitive to radar beam attenuation, ground clutter contamination and unsubstantial variations in the DSD compared to Z. Studies such as [11], [16], [18] have adopted the use of K_{DP} for QPE at X-Band and found higher efficacy for a variety of precipitation regimes. [16] further demonstrated that K_{DP} corrected $Z - R$ relation provides improvement over using K_{DP} or Z alone. Previous studies have also explored the use of hybrid estimators that uses a hydrometeor classification scheme to guide the application of appropriate rainfall estimators that

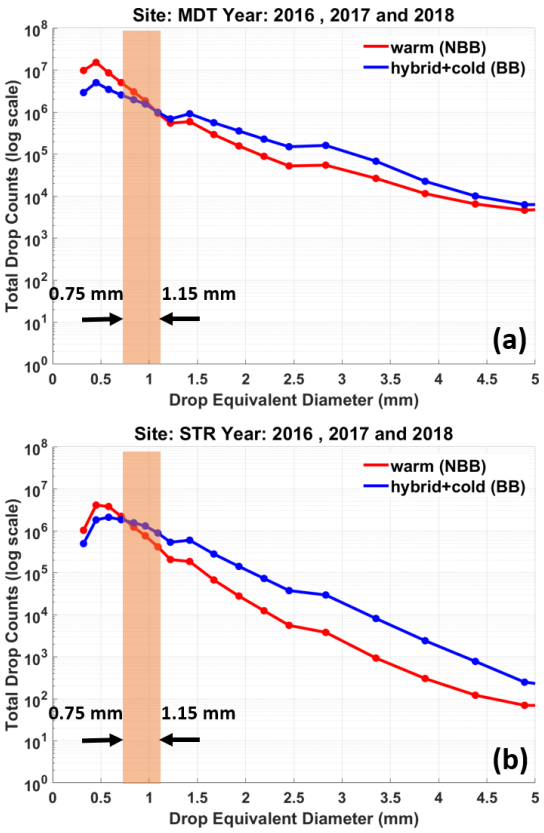

Fig. 3. Total drop counts vs drop equivalent diameter in NBB rain and BB rain at (a) MDT site and (b) STR site based on data from the 2016 - 2018 rain seasons. The shaded region in (a) and (b) indicates the crossover between small and large sized drops.

best fits the precipitation type [2], [19], [20]. However, in areas of complex terrain, especially in coastal regions, DSD is found to be highly variable on spatial and temporal scales as reported by [9]–[11]. Under such conditions, a fixed Z-R relationship can produce large errors since Z is highly sensitive to DSD variation [17], [21]. Regardless of having greater accuracy in comparison to Z-R based estimation, fixed $R(K_{DP})$ based rainfall measurements can also be affected by both spatial and temporal variation in the DSD in cases of orographic induced rain combined with stratiform rain. Changes in DSD governs the modifications of coefficients between rainfall rate and various radar observable. Hence, a fixed $R(Z)$ or $R(K_{DP})$ can not reasonably represent the fine scale variability of the DSD.

Previous studies have focused on radar based precipitation estimation, forecasts and validation of numerical models over the San Francisco Bay Area [22]–[27]. However, study radar based QPE for this region focusing on orographic rainfall has not been done yet. The main objective of this work is to determine a hybrid QPE algorithm that would support the Advanced Quantitative Precipitation Information (AQPI) System [28]. This algorithm would account for the influence of NBB rainfall on polarimetric rainrate estimators at X-Band and is also expected to improve existing QPE products in this region. In this study, collocated Parsivel disdrometer and S-PROF measurements from two NOAA HMT sites are used. The Santa Rosa site is located in the coastal plains in the Russian River valley whereas the Middletown site is located in the adjacent mountains. Microphysical characteristic of cold season stratiform or BB rainfall and orographically forced NBB rainfall are studied using rain events from 3 years 2016 to 2018. DSD samples corresponding to rainfall delineated by presence and absence of bright-band is classified into two broad categories namely BB and NBB. Further investigation revealed specific characteristics of BB rain and NBB rain in agreement with previous studies as described above. Subsequently, DSD spectra are used to calculate radar variables at X-Band by T-Matrix scattering method [29]. An empirical relationship based on $Z - Z_{DR}$ is developed in order to differentiate between these two rain types that can be used on real X-Band radar data. Corresponding polarimetric radar rainfall estimators are also constructed. When applied to the X-Band radar data this method showed improvement in QPE compared to existing products. This study discusses the development of an accurate X-Band based QPE methodology focusing on orographic rainfall for the AQPI system, as well as the growing body of literature focusing on remote sensing of precipitation in complex terrain.

This paper is organized in the following manner. Section II presents a detailed discussion on stratiform and orograhic rain followed by quantitative analysis of various datasets used in this study. Section III provides applications of dual polarization radar rainfall estimation in stratiform and orographic rain followed by Section IV which presents QPE comparison results from selected case studies of precipitation events. In the end, Section V summarizes the QPE methodology for orographic rain presented in this study along with discussions on limitations and future scope of the proposed methodology.

II. Data and Methods

A. Study Domain and Instruments

The Advanced Quantitative Precipitation Information (AQPI) project is a joined effort by the California Department of Water Resources (DWR), Sonoma Water, the National Oceanic and Atmospheric Administration (NOAA), Cooperative Institute for Research in the Atmosphere (CIRA) and a multitude of universities and local government agencies. It aims to improve weather monitoring, forecast, streamflow prediction, and coastal flood warning in the San Francisco Bay Area. As a part of this project, a state of the art system has been developed that features gap filling X-Band dual polarization radars and advanced surface observational instruments and flooding models [22], [28]. The AQPI domain spans over approximately 76300 km^2 of area which covers most of the flood prone watersheds in this region. The future goal is to develop an operational radar network consisting of four gap filling X-Band dual polarization radars and deployment of a C-Band dual polarization radar at the coast to observe approaching storms over the ocean. Recently, two X-band radars namely XSCW and XSCV have been deployed at Santa Rosa and Santa Clara respectively. These radars are expected to augment existing NEXRAD coverage and provide detailed understanding of rainfall processes. This study is focused on

the region of the Russian River watershed observed by the XSCW radar in Sonoma County, California. NOAA's Hydrometeorology Testbed (HMT) program, co-managed by OAR Physical Sciences Laboratory (PSL) and National Weather Service (NWS) Weather Prediction Center, also includes several ground based observation sites in California. Most of these sites are equipped with tipping bucket rain gauges and optical disdrometers, while few of them also have a vertically pointing S-Band Profiler (S-PROF) radars.

TABLE I
INSTRUMENT SITE INFORMATION

Station ID	Lat.	Lon.	Elv. (MSL)
XSCW	38.5216^oN	122.8022^oW	$38.5m$
STR	38.5154^oN	122.8022^oW	$32m$
MDT	38.7456^oN	122.7112^oW	$972m$

Figure 1a shows a terrain map of Sonoma County area along with location of the XSCW X-Band radar and NOAA HMT surface instrumentation sites. The black circles represent radar observation ranges starting from 0 to 40 km with 10 km increment. The red crosses represent two NOAA HMT sites named STR located at Santa Rosa and MDT located at Middletown. Both locations contain S-PROF, Parsivel disdrometers and surface observation gauges. Figure 1b and Figure 1c shows the XSCW radar beam along the line of sight azimuth direction of the two HMT sites. The azimuth and distance between the radar location and HMT sites is shown on the image. The STR site is located in the valley very close to the radar whereas the MDT site is located in the mountains near the eastern boundary of the watershed. The distance between the two sites is 27 km. Table I presents latitude/longitude and elevation information of all the sites. For analysis purposes, data from collocated Parsivel disdrometer and S-PROF radars at the STR and MDT sites are selected corresponding to the 2016 to 2018 rainy season.

B. Rainfall Type Classification based on S-PROF Observations

Stratiform rain occurs when when precipitation extends above the freezing level. In this type of rain, below 0^o C, hydrometeors consist of aggregated snowflakes. As the aggregates fall and encounter the melting layer, they start to melt from the outside. At this point, frozen hydrometeors develop a outer coating of water and they appear to the radar as large drops of liquid. Since the radar reflectivity factor is sensitive to the sixth power of the drop diameter, there is a large increase in Z_H at the melting layer. It is also accompanied by decrease in both differential reflectivity Z_{DR} and co-polar coherency ratio ρ_{HV}. This phenomenon is known as the radar bright-band signature. Hence, stratiform rain is also termed as BB rain. Below this region, the drops completely melt to liquid and break into smaller drops due to aerodynamic instability. In contrast, orographic rainfall is associated with warm rain process when rainfall is shallow and enhanced by topography. In this case, precipitation is mostly present below the melting layer with the absence of large snowflake aggregates. A myriad of water drops grow to moderate sizes by condensation aided by up-slope flow and by coalescence of drops in a relatively shallow layer near the terrain. Orographic rain usually exhibits lower reflectivity values compared to stratiform rain due to presence of large concentration of smaller drops. Due to the spherical nature of small drops, for this type of rain, differential reflectivity values are very low (less than 0.5 dB) accompanied with very high correlation coefficient. In this study, both the stratiform and orographic rain are found to be dominant in the Sonoma County region. [9] used vertically pointing S-PROF radar measurements to classify different rainfall types in half hour periods based of profile by profile analysis. The S-PROF radars generate measurements of vertical profile of reflectivity and Doppler velocity with a spatial resolution of 60 meter and typically are updated every 1 minute interval. The different categories in that study were warm rain, cold rain, hybrid rain, and convective rain. If several different rainfall types were observed during a particular half hour period, the rain type with more clearly defined profiles was assigned to the entire period. For analysis purposes, BB rain is considered a single category without subdividing it into cold and hybrid rain since both of these rain types exhibits bright band signatures. Warm or orographic rain on the other hand is considered as NBB rain. In the dataset considered for this study, the convective rain periods accounted for less than 5% of the total rainy period and therefore are excluded. As the bright band signature is usually obscured in convective rain, it can also be regarded as NBB rain. However, since convective rain is not examined in this study, the NBB terminology solely refers to warm or orographic rain.

C. DSD Characteristics

DSD spectra collected from disdrometers are useful in identifying bulk microphysical properties of precipitation. The NOAA HMT Parsivel disdrometers are configured with a sampling resolution of 10 second. Each of these samples contains detected number of raindrops within the sampling interval which is arranged in a 32 by 32 drop size versus fall velocity matrix. This information represents the DSD spectra. The diameter size ranges from 0 to 25 mm with individual bin width increasing with the size from 0.125 to 3 mm. Detectable fall velocity values ranges is from 0 to 20 m/s with each bin width increasing with fall velocity. Detailed technical information about Parsivel disdrometers can be found in [30]. If each velocity bin is denoted by i and diameter bin is denoted by j then the total number of raindrops D_{tot} can be calculated as

$$D_{tot} = \sum_{i=1}^{32}\sum_{j=1}^{32} n_{i,j} \tag{1}$$

where $n_{i,j}$ stands for number of drops in each bin. In order to improve data reliability of the raw samples a series of data quality control procedure have been applied. First, each 10 second sample are aggregated to 2 minute intervals to minimize random sampling errors. These 2 minute samples help to better comprehend overall rainfall characteristics. In addition, raindrops from the lowest two bins are rejected due

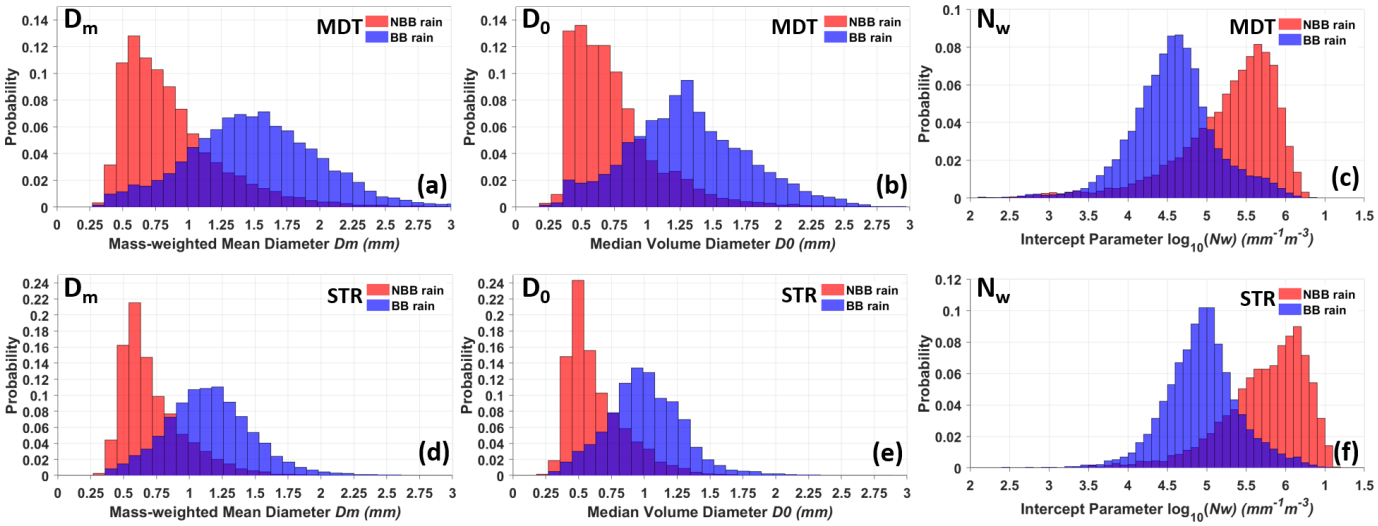

Fig. 4. Histograms of (a,d) D_m, (b,e) D_0, and (c,f) $log_{10}N_w$ at the (top) MDT and (bottom) STR sites calculated from DSD data from the 2016 - 2018 rain seasons.

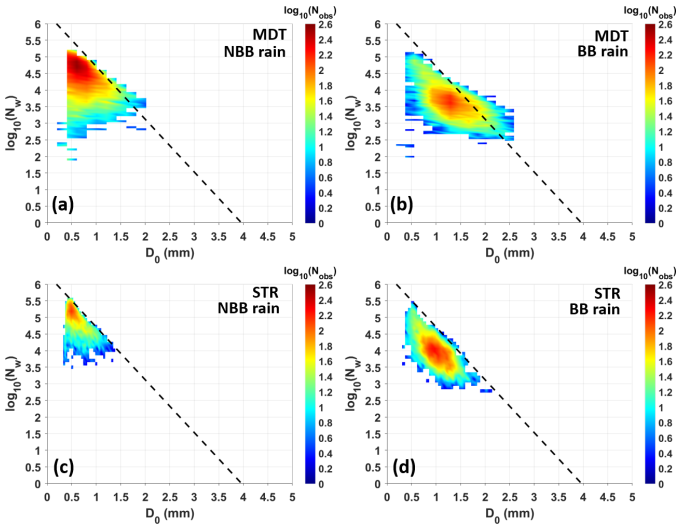

Fig. 5. Scatter density plots of $log_{10}N_w$ versus D_0 in (a,c) NBB and (b,d) BB rain at the (top) MDT and (bottom) STR sites. The black dashed line signifies stratiform and convective separation based on equation 12

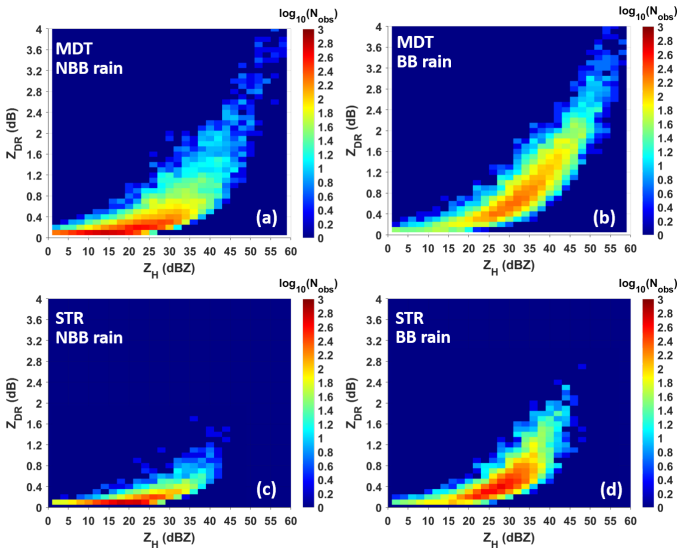

Fig. 6. Scatter density plots of Z_{DR} versus Z_H in (a,c) NBB and (b,d) BB rain at the (top) MDT and (bottom) STR sites, calculated from the 2 minute DSD samples using T-Matrix scattering method.

to low signal-to-noise ratio. DSD spectra with total number of drops less than 20 as well as spectra with derived rainfall rate less than 0.1 mm/h are removed from the analysis [31]. Furthermore, raindrops of diameters larger than 8 mm are not considered in order to avoid hail contamination according to [17]. Finally, the empirical terminal fall velocity versus drop diameter (V-D) relationship by [32] is adopted to mitigate contamination introduced by strong horizontal wind gradient and partially melted hydrometeors.

$$V(D) = 9.65 - 10.3e^{-0.6D} \tag{2}$$

Velocity measured by the disdrometer is compared to the Atlas relation in equation 2 for each diameter bin. Drops with measured velocities within a $\pm 50\%$ error are considered for further analysis. All of the above data quality control methods are applied to essentially restrict data to rain samples only. A total of 63,033 raw samples were studied out of which only 36,421 samples passed the quality control criteria. Figure 2 shows disdrometer data from 2016 to 2018 at STR and MDT sites before and after the quality control process. The number concentration of raindrops per unit volume for the j^{th} diameter bin can be calculated according to

$$N(D_j) = \sum_{i=1}^{32} \frac{n_{i.j}}{A\Delta t V_i \Delta D_j} \tag{3}$$

where $N(D_j)$ is in $m^{-3}mm^{-1}$; D_j is the j^{th} diameter bin in mm; A is the sampling area of the disdrometer which is 0.0054 m^2; Δt is the sampling time interval which is 120 seconds; ΔD_j is the width of j^{th} diameter bin in mm; V_i is the value of fall speed for the i^{th} velocity bin in ms^{-1}. Rainfall rate R

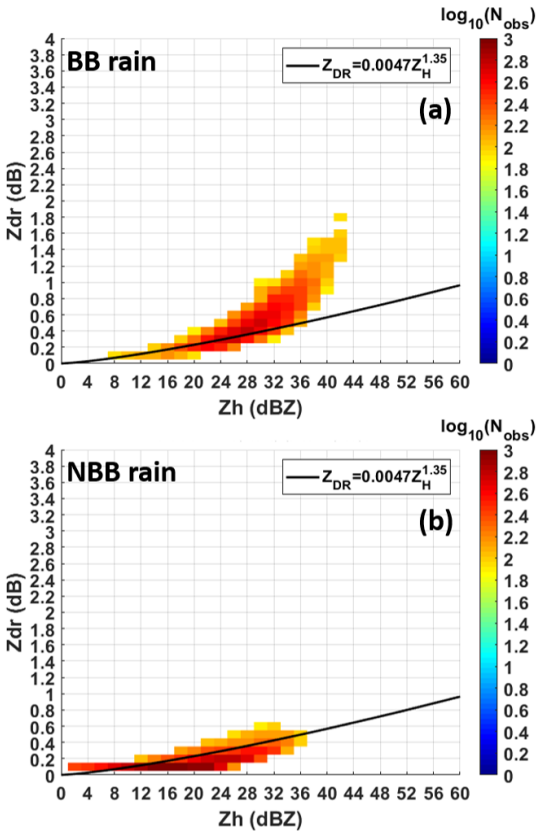

Fig. 7. Classification of NBB versus BB rain in Z_{DR} versus Z_H space using the empirical relation in 13 denoted by a black curve. (a) Z_{DR} versus Z_H scatter density plot for BB rain samples computed from DSD data from STR and MDT sites combined (b) Same as (a) but for NBB rain samples. It should be noted that only grid points with sample density greater 50 are considered.

$(mm\ h^{-1})$ can be calculated based on $N(D)$ as

$$R = 6\pi \times 10^{-4} \sum_{j=1}^{32} V(D_j) D_j^3 N(D_j) \Delta D_j \tag{4}$$

where $V(D_j)$ is the velocity at the jth diameter bin calculated using 2. Furthermore, a normalized gamma DSD model first reported by [33] has been adopted in this study for calculating the median volume diameter D_0 (mm), mass-weighted mean diameter D_m (mm), and intercept parameter N_w $(m^{-3}\ mm^{-1})$. The normalized gamma DSD can be described as

$$N(D) = N_{\mathrm{w}} f(\mu) \Big(\frac{D}{D_m}\Big)^{\mu} \exp\Big[-(4+\mu)\frac{D}{D_m}\Big] \tag{5}$$

Here, $f(\mu)$ is given by

$$f(\mu) = \frac{6(4+\mu)^{\mu+4}}{4^4 \Gamma(\mu+4)} \tag{6}$$

where μ is the shape parameter and Γ is the Euler Gamma function. D_m can be expressed as a ratio of the fourth-order moment of $N(D_j)$ to the third-order moment of $N(D_j)$ as follows:

$$D_m = \frac{m_4}{m_3} \tag{7}$$

where the nth-order moment m_n of $N(D_j)$ is defined as

$$m_n = \sum_{j=1}^{32} D_j^n N(D_j) \Delta D_j \tag{8}$$

The median volume diameter D_0 is defined such that drops smaller than D_0 contribute to half the total liquid water content W $(g\ m^-3)$ as follows

$$\int_0^{D_0} D^3 N(D) dD = \frac{1}{2} \int_0^{\infty} D^3 N(D) dD = \frac{1}{2}(W) \tag{9}$$

It is also related to D_m as

$$\frac{D_0}{D_m} = \frac{3.67+\mu}{4+\mu} \tag{10}$$

N_w is calculated as

$$N_{\mathrm{w}} = \frac{4^4}{\pi}\Big(\frac{10^3 W}{D_m^4}\Big) \tag{11}$$

It should be noted that rainfall accumulations of individual events from 2016 to 2018 for Parsivel disdrometer data and the collocated tipping-bucket type rain gauges were generally in agreement to within $10\%-15\%$. A close agreement of Parsivel rainfall rate retrievals and those from the robust 2D video disdrometer measurements was also reported by [34]. These gives an additional indication of the suitability of using the Parsivel disdrometer data. The quality controlled DSD samples are classified into BB and NBB rainfall categories according to the simultaneous observations from the collocated S-PROF at STR and MDT site. Figure 3 represents total drop counts vs drop equivalent diameters at both sites. In this study, drops below 1.5 mm diameter are considered as small drops. Drops of diameter between 1.5 - 3 mm are considered as mid-sized drops and drops greater 3 mm are considered as large drops according to [30], [35]. It is observed that NBB rain has a higher frequency of small rain drops at both sites, while BB rain has a higher frequency of mid-sized to big drops. The crossover from small drops to mid-sized and larger drops is between 0.75 - 1.15 mm drop diameter for both sites. There is a bigger separation from mid-sized to large drops at STR compared to MDT. In addition, MDT has a higher number concentration of smaller drops compared to STR suggesting dominance of orographic process due to abrupt lifting of air by local mountainous topography. These features are further demonstrated by the probability distribution of mass-weighted mean diameter D_m, median diameter D_0 and normalized intercept parameter N_w in Figure 4. In this figure, BB rain is denoted by blue and NBB rain is denoted by orange. D_0 and D_m both have similar positively skewed distributions in BB and NBB rain. It can be seen that, although there is some overlap, NBB rain in general has a higher probability of smaller drop diameter compared to BB rain whereas BB rain has a higher probability of bigger drop diameter. The N_w distribution of NBB rain is negatively skewed at both sites while the distribution of N_w in BB rain is symmetric. This supports the findings in Figure 3 that NBB rain has higher concentration of overall drops counts compared to BB rain.

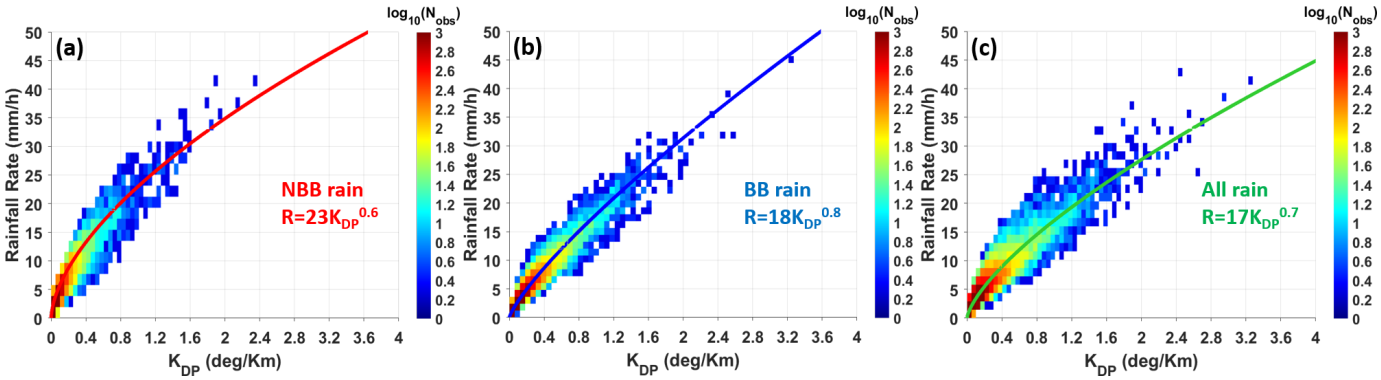

Fig. 8. Rainfall Rate R versus Specific Differential Phase K_{DP} from disdrometer observations at the STR and MDT sites combined (a) for NBB rain samples (b) for BB rain samples (c) for both BB and NBB rain samples considered together

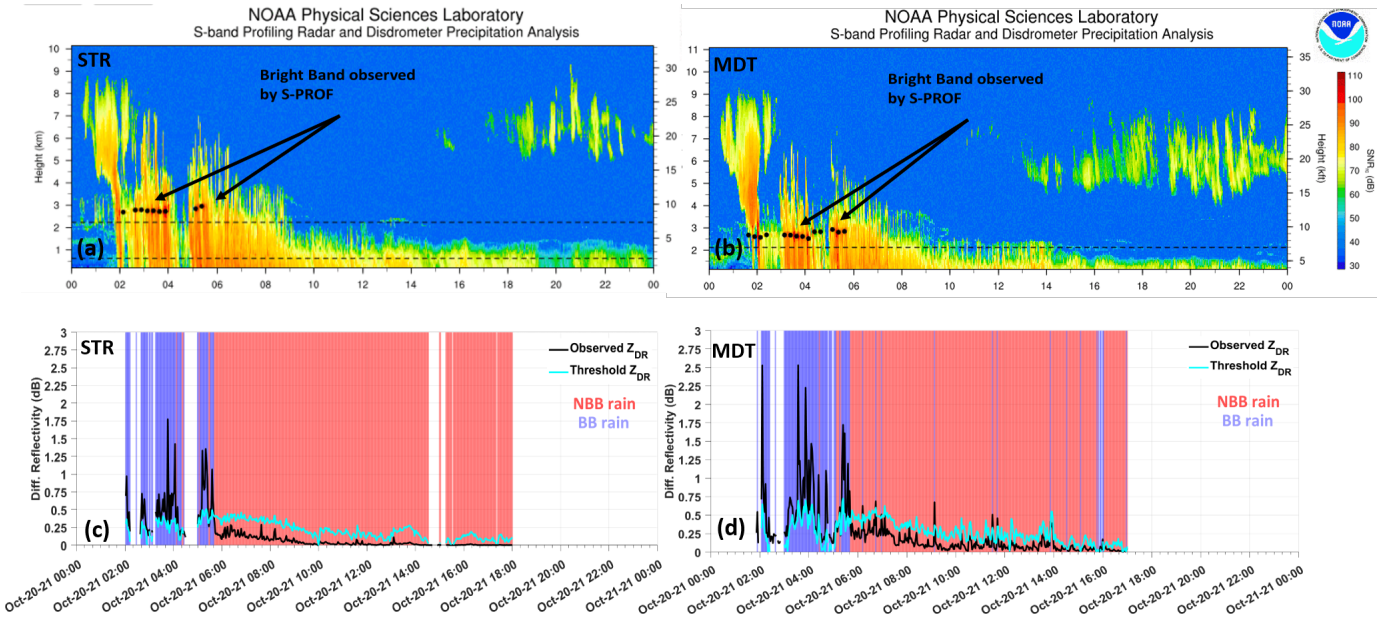

Fig. 9. (a-b) Images of S-PROF radar Signal to Noise Ratio (SNR) at the STR and MDT site for October 20 2021 precipitation event. The black dots in bold represent the S-PROF radar derived snow level. The thin black dashed lines represent the NEXRAD KDAX beam heights. These images are taken from the website "https://psl.noaa.gov/data/obs/datadisplay/". (c-d) Classification of BB versus NBB rain at the STR and MDT site using dual-pol XSCW radar observations for the October 20 2021 precipitation event. The black and light blue solid lines represent observed Z_{DR} and threshold Z_{DR} which is calculated using equation 13 respectively. Periods of BB rain is shaded in blue while NBB rain is shaded in red.

Figure 5 presents scatter density plots of $log_{10}N_w$ versus D_0 for BB and NBB rain at the two sites. The black dotted line is used to separate stratiform region from convective region in the $log_{10}N_w$ versus D_0 sample space [36], [37]. The equation of line is given by

$$log_{10}N_w^{sep} = -1.6D_0 + 6.3 \tag{12}$$

where N_w^{sep} indicates the threshold value of N_w for classifying stratiform rain from convective rain corresponding to a median volume diameter D_0. As expected, almost all samples fall in the stratiform region. In summary, it can be concluded that, NBB rain observations at both sites exhibit higher concentration of smaller drops compared to BB rain. For both rain type the mean values of D_0 are larger at MDT compared to STR. Dominance of orographic enhancement at MDT is clearly indicated due to a higher concentration of small drops.

III. Dual Polarization Radar Applications

Even though it is relatively straightforward to distinguish BB rain from NBB rain using profiles of Z and Doppler velocity observations from vertical pointing profilier radars, it is a bit challenging to perform the same classification using PPI scans in case of weather radars. Previous works by [38]–[40] focused on bright-band detection and VPR correction using polarimetric scanning radar data. [11] demonstrated the possibility of using polarimetric radar variables at S-Band for identifying BB and NBB rain types. However, polarimetric relations at X-Band has not been explored yet. This study focuses on developing a robust methodology for delineation of stratiform or BB rain from orographic or NBB rain that can be applied to scanning X-Band radar data in real time.

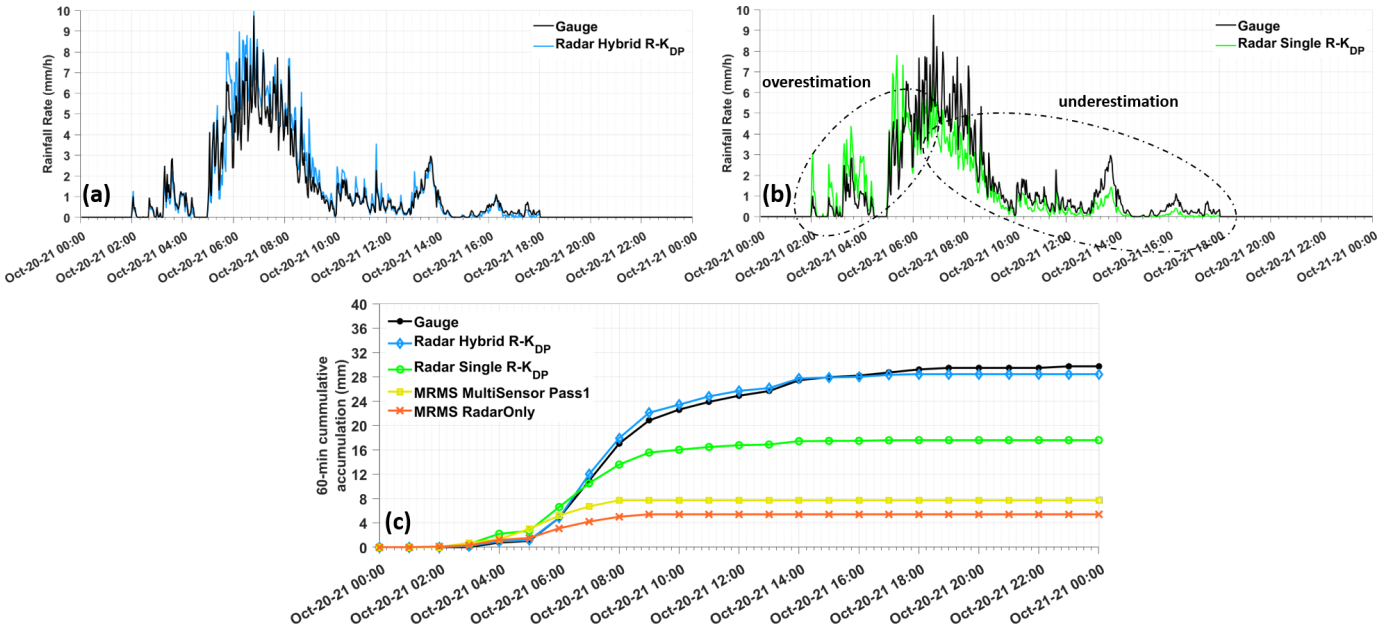

Fig. 10. Comparison of different rainfall products with rain gauge at the STR site for the October 20 2021 precipitation event. (a) Rainfall Rate using hybrid $R(K_{DP})$ vs gauge rainfall (b) Rainfall Rate using a single $R(K_{DP})$ relation vs gauge rainfall. (c) Cumulative accumulation of hourly rainfall at the STR rain gauge location from different rainfall products.

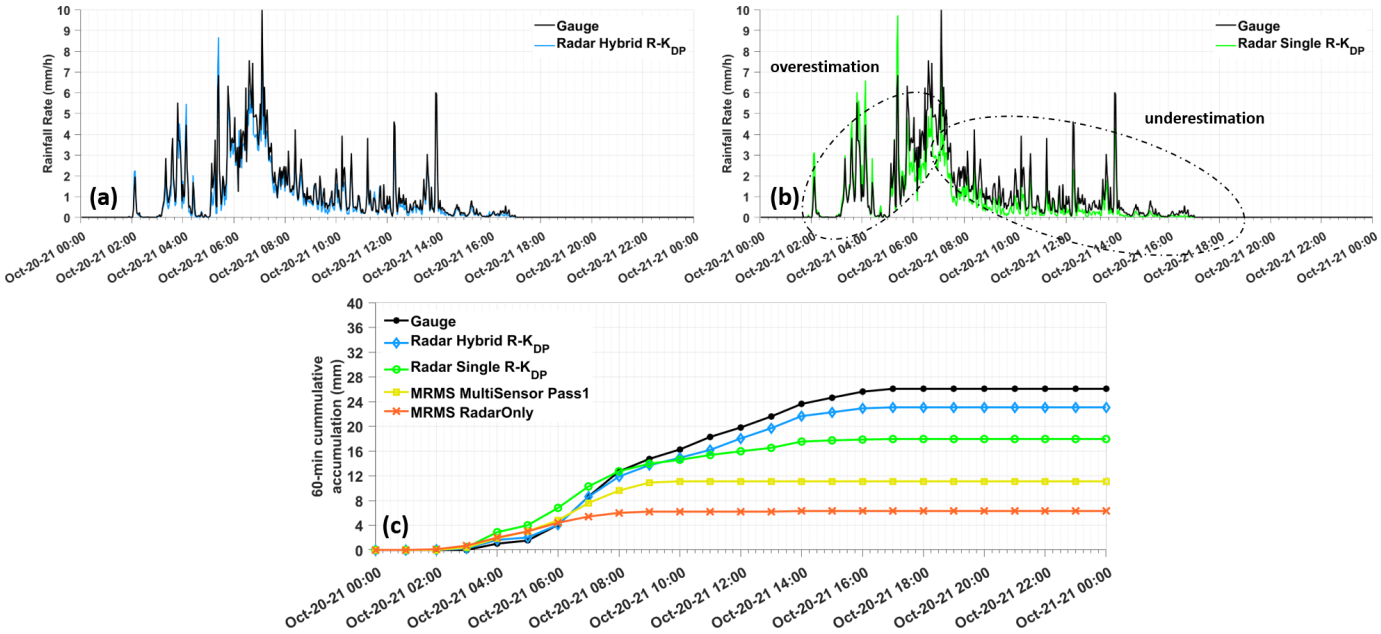

Fig. 11. Comparison of different rainfall products with rain gauge at the MDT site for the October 20 2021 precipitation event. (a) Rainfall Rate using hybrid $R(K_{DP})$ vs gauge rainfall (b) Rainfall Rate using a single $R(K_{DP})$ relation vs gauge rainfall. (c) Cumulative accumulation of hourly rainfall at the MDT rain gauge location from different rainfall products.

A. Classification of BB and NBB rain type using dual-pol radar parameters at X-Band

Polarimetric radars are sensitive to drops shapes. Higher concentration of small drops in NBB rain signifies the dominant drop shapes observed in radar resolution volume will be more spherical than in BB rain. Hence, polarimetric radar has potential to detect different rain types as well as provide more accurate estimates of rainfall intensity than usually possible with single polarization measurements [17]. In Rayleigh scattering, the particle sizes are much smaller compared to the radar wavelength. In this case, the radar reflectivity factor can be shown approximately equivalent to the sixth moment of the drop size distribution. However this assumption often time fails in the case of large drops at a wavelength of 3 cm corresponding to X-Band. Therefore, in this study, dual polarization parameters specific differential phase K_{DP} $(deg.km^{-1})$ and differential reflectivity Z_{DR} (dB) along with reflectivity at horizontal polarization Z (dBZ) were computed

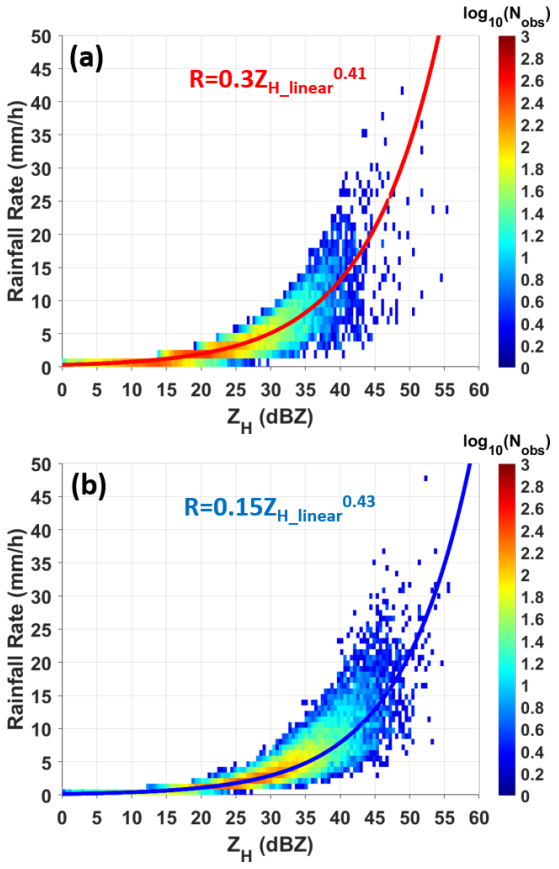

Fig. 12. Rainfall Rate R versus Reflectivity Z in BB and NBB rain

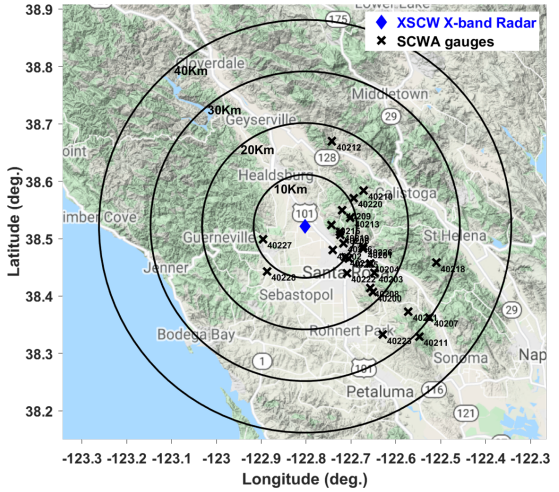

Fig. 13. Location of rain gauges within the 40 km range domain of the XSCW radar usde for validation purposes in this study. These rain gauges are maintained by the Sonoma County Water Agency

using the T-Matrix scattering method [29]. Quality controlled two minute DSD samples classified into BB and NBB rain are used for the computation assuming a Gamma distribution. Drops are assumed to be symmetric with orientation canting angle following a Gaussian distribution with zero mean and standard deviation of 5^o. The drop shape model described in [41] has been used. The calculated Z and Z_{DR} in BB and NBB rain from DSD samples at both sites are presented in Figure 6 in form of scatter density plots. It can be observed the distributions of Z_{DR} vs Z are significantly different for NBB compared to BB rain. The Z and Z_{DR} values for BB rain are higher compared to NBB rain. About 95% of the Z_{DR} values for NBB rain are less than or equal to 0.5 dB suggesting larger fraction of smaller spherical drops. A polarimetric approach is implemented for identifying NBB rain and BB rain based on the observed Z_{DR} versus Z pattern. As observed from the Z_{DR} versus Z plots in Figure 6, it is apparently difficult to distinguish the two rain types by a single Z or Z_{DR} threshold due to some overlap of BB and NBB samples. About 15% of the total samples are overlapped in the region of $8\ dBZ \leq Z \leq 36\ dBZ$ and $0.35\ dB \leq Z_{DR} \leq 0.6\ dB$. This can be better visualized in the Figure 7 which is a scatter density plot of Z_{DR} vs Z computed from the disdrometer samples from STR and MDT sites combined. This figure is constructed with pixels of sample density exceeding 50 in order to clearly visualize the difference in distributions. An empirical relation given by the equation

$$Z_{DR}^t = 0.0047 Z^{1.35} \tag{13}$$

is proposed based on a fit to the data. It can be observed from Figure 7 that the black curve represented by equation 13 is able to separate the BB and NBB rainfall types. For a given value of Z the threshold Z_{DR} value for BB-NBB separation is denoted by Z_{DR}^t. If the observed Z_{DR} value is greater than this threshold, it is classified as BB rain and the opposite is true for NBB rain. In Figure 7, about 85% of the rain samples of either rainfall type can be accurately classified by equation 13. However, the classification of the remaining 15% samples is ambiguous due to sample overlap which is discussed earlier. It is emphasized that this approach is only applicable to radar observations of rain where there is no contamination from mixed phase and ice hydrometers.

B. Dual-pol rainrate estimators for BB and NBB rain type at X-Band

Rainfall rates R are retrieved by summation of individual rainfall rate at each disdrometer's diameter bin using equation 4. The calculated K_{DP} values and the corresponding rainfall rates from the DSD data are segregated for the two types of rain. Scatter density plots of R versus K_{DP} were made to get an overall trend of the rainfall rates compared to K_{DP}. This is shown in Figure 8a and b. The distributions were then fitted using an exponential curve which yielded two distinct equation. These two $R(K_{DP})$ estimators are given by

$$\begin{aligned} R_{BB} &= 18 K_{DP}^{0.8} \\ R_{NBB} &= 23 K_{DP}^{0.6} \end{aligned} \tag{14}$$

Since most of the K_{DP} values for the two types of rain are less than 1 deg/km, a lower exponent, as in the case of NBB rain estimator, means higher rainfall rate compared to the BB one. Figure 8c shows the density plot between rainfall rate versus K_{DP} when both BB and NBB samples are considered together. An exponential fit is also made to this distribution which is given by the equation

$$R = 17 K_{DP}^{0.7} \tag{15}$$

TABLE II
SONOMA COUNTY WATER AGENCY RAIN GAUGE LOCATION

Gauge ID	Lat. (deg.)	Long. (deg.)	Location
'40200'	38.406656	-122.651431	Matanzas Reservoir
'40201'	38.482242	-122.672988	Brush Creek
'40202'	38.479830	-122.740988	Piner Creek
'40203'	38.440170	-122.648364	Spring Creek
'40204'	38.457047	-122.657442	Spring Lake
'40206'	38.506803	-122.723863	Linda Creek
'40207'	38.362584	-122.525253	Sonoma Creek
'40208'	38.413978	-122.657462	Matanzas Creek
'40209'	38.549400	-122.720072	Mark West Creek
'40210'	38.583716	-122.671742	Franz Creek
'40211'	38.329098	-122.547601	McCrea Trail Parcel
'40212'	38.669962	-122.742251	Buckeye Creek Ranch
'40213'	38.535928	-122.701547	Mark West Regional Park
'40215'	38.523822	-122.743892	Shiloh Ranch Regional Park
'40216'	38.492002	-122.717053	Skyfarm Water Tank
'40217'	38.467749	-122.712766	Paulin Creek
'40218'	38.458215	-122.510119	Bald Mountain
'40219'	38.511754	-122.724335	Mark West Creek
'40220'	38.570609	-122.694050	Pepperwood Preserve
'40221'	38.372593	-122.572176	Enterprise Road
'40222'	38.439661	-122.708967	Santa Rosa Downtown Culverts
'40223'	38.332678	-122.629408	Copeland Creek
'40225'	38.465531	-122.704673	Piner Creek Dam
'40226'	38.486643	-122.672493	Brush Creek Middle Fork Dam
'40227'	38.499188	-122.896077	Mirabel
'40228'	38.442742	-122.887214	Green Valley

It is interesting to note that this exponential fit is quite different from either of NBB and BB rains. The exponent lies between that of NBB and BB equations suggesting that it is an overall average fit. To demonstrate the significance of the hybrid $R(K_{DP})$ estimators on QPE, an orographic precipitation event on Oct 20, 2021 is chosen for analysis. Figure 9 shows BB vs NBB classification at the STR and MDT sites following the method developed in this study. Figure 9a and 9b are images of the S-SPROF radar SNR at the STR and MDT site respectively. The image is taken from the NOAA PSL web display. Figure 9c and 9d shows time series of measured Z_{DR} at the two sites. The black line depicts observed Z_{DR} whereas as the light blue line denotes the Z_{DR} threshold calculated from the relation in equation 13. The blue shaded periods correspond to BB rain whereas the orange shaded periods corresponds to NBB rain. The classification based on X-Band dual-pol observations in Figure 9c and d is found to be consistent compared to the S-PROF observations. Occurrence of BB rain can be observed approximately until around 06:00 UTC, after which it is all NBB rain. The hybrid $R(K_{DP})$ estimator is applied according to the rainfall type classification and subsequently rainfall accumulations are calculated for each hour for the whole event at both sites. Hourly rainfall accumulations are also calculated using the average $R(K_{DP})$ relation, given by equation 15. The radar estimates are compared against the tipping bucket rain gauges present at both sites. In addition, two operational QPE products namely the MRMS MultiSensor Pass1 and MRMS RadarOnly are also compared. Detailed description of the MRMS products can be found in [20] and [42]. Both of these operational products provide hourly estimates of rainfall over the CONUS. Figures 10 and 11 both show comparison of the hourly rain gauge measurements with radar rainfall estimates computed using equations 14 and 15. It is interesting to note that, both in figures 10b and 11b that the hourly rainfall estimates calculated using the average $R(K_{DP})$ slightly overestimates during the BB periods with significant underestimation during the NBB periods. In contrast, the radar estimates using the hybrid $R(K_{DP})$ estimators, as shown in figures 10a and 11a, performs very well. This can be observed in the rainfall cumulative accumulation comparison in figures 10c and 11c. Both of the MRMS QPE products as well as the rainfall estimate using average $R(K_{DP})$ tends to significantly underestimate.

Oftentimes, at very low rainfall rate the estimated K_{DP} from radar observations of differential phase can be very noisy. In addition, K_{DP} can be affected by bright band contamination when the lowest radar scans are intersected by the melting layer being very close to the ground [17]. In these scenarios, it is not advisable to use K_{DP} for estimating rainfall and use Z instead. In case of bright band contamination, appropriate correction of the reflectivity vertical profile should be performed before using $R(Z)$ estimator. Thus, apart from the $R(K_{DP})$ relations, $R(Z)$ relations for both BB and NBB rain are also developed using the disdrometer measurements. They are given by

$$R_{BB} = 0.15 Z_{lin}^{0.43}$$
$$R_{NBB} = 0.3 Z_{lin}^{0.41} \quad (16)$$

where Z_{lin} is reflectivity in linear units $(mm^6\ m^{-3})$. Figure 12 present the $R(Z)$ estimators.

IV. EVALUATION USING CASE STUDIES

Observations from the XSCW X-Band radar have been used to test the performance of the hybrid rainfall relations, developed in the previous section, against independent rain gauges. The radar is located in Santa Rosa and provides PPI scans starting at elevation of 1.5^o and ending at 4.5^o with 1 degree intervals. This radar observed several orographic precipitation events in the year 2021. For comparison purpose, three significant events are chosen consisting of low, moderate to heavy rainfall accumulations. The first event is from January 27-28 2021 which produced moderate rainfall amounts. During this event, the environmental freezing level was very close to the ground which was about 1 km. The other two events are from October 20 2021 and October 24 2021. Both of these events had significant orographic enhancements as observed by the S-PROF radar. The October 24 2021 event was the highest rainfall producing event of the year in this region, whereas the October 20 2021 event exhibited lower rainfall rates compared to the other two events. Radar based rainfall estimates are compared with simultaneous measurements from rain gauges maintained by Sonoma County Water Agency (SCWA). There are a total of 26 rain gauges which are used in this analysis. Figure 13 shows the location of the gauges within the radar 40 km range domain. Table II shows the different SCWA gauge IDs along with their location and geographic coordinates. The

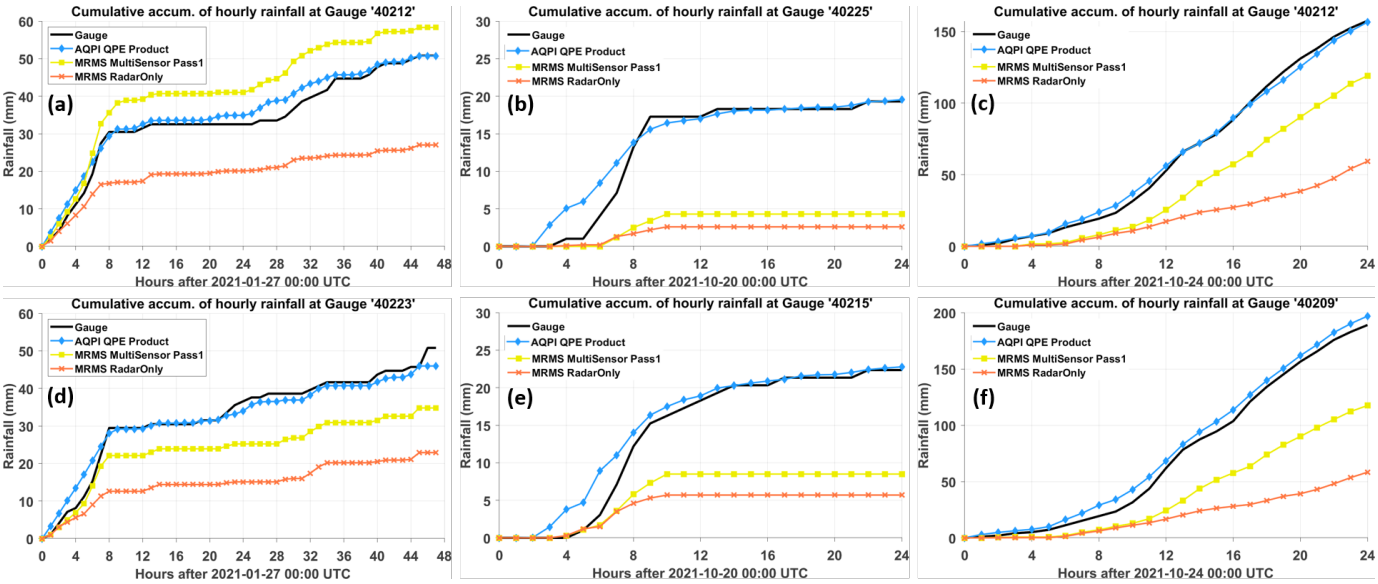

Fig. 14. Comparison between cumulative accumulation of hourly rainfall for whole event at SCWA (a,d) gauge ID 40212 and 40223 for the January 27-28 2021 event, (b,e) gauge ID 40225 and 40215 for the October 20 2021 event, and (c,f) gauge ID 40212 and 40209 for the October 24 2021 event. Blue line indicates the AQPI XSCW radar product using hybrid rainfall estimation algorithm, the yellow line indicates the MRMS Multisensor Pass 1 product and the orange line indicates the MRMS RadarOnly Product.

TABLE III
STATISTICAL METRICS

		Mean Bias (mm)	Mean Absolute Error (mm)	Root Mean Square Error (mm)
Jan 27-28 2021	**R-KDP Hybrid**	-0.17	6.78	10.00
	MRMS MultiSensor Pass1	-1.78	10.37	13.00
	MRMS RadarOnly	-22.78	22.00	26.20
Oct 20 2021	**R-KDP Hybrid**	0.48	2.92	3.75
	MRMS MultiSensor Pass1	-12.08	12.11	12.8
	MRMS RadarOnly	-14.32	14.32	15.13
Oct 24 2021	**R-KDP Hybrid**	-3.6	19.6	22.99
	MRMS MultiSensor Pass1	-71.89	71.89	75.93
	MRMS RadarOnly	-123.42	123.42	125.4
All events	**R-KDP Hybrid**	-1.15	8.91	12.76
	MRMS MultiSensor Pass1	-28.86	31.79	45.44
	MRMS RadarOnly	-54.24	54.24	75.10

methodology developed in this study first classifies rainfall into BB and NBB category using Z and Z_{DR} observations at each radar range gate. It very crucial that both Z and Z_{DR} should be well calibrated and free of systematic bias. The bias estimation is performed by comparing Z calculated from the STR disdrometer measurements and the actual observed Z by the radar. Since the dual-pol radar variables are calculated from the disdrometer observations using a computed scattering table, they are regarded as true values. The mean Z bias for all the 3 events was found to be -5 dBZ indicating the radar Z is lower by 5 dBZ. Therefore, an adjustment of +5 dBZ was applied. For Z_{DR} bias, two methodologies were followed. The first one is a comparison with disdrometer which was carried out in a similar manner like the Z bias estimation. The second one is performed by the method of observation of drizzle at very low elevation angle. In this study observations from the lowest PPI scan angle of 1.5^o was used. In order to select drizzle, both Z and Z_{DR} was masked with signal to noise ratio (SNR) greater than 15 dB and correlation coefficient (ρ_{HV}) greater than 0.99. In addition, only Z values between 0 and 15 dBZ are considered. With these criteria, Z_{DR} values are selected for bias estimation. In theory, the Z_{DR} in this scenario should be a Gaussian with a mean of 0 dB. Any deviation from the 0 dB mean is taken as the bias. For all the three events, the mean Z_{DR} bias was found to be 2.5 dB from the two individual procedures mentioned above. Next, the classification methodology is applied to radar scanning data collected at 2.5^o elevation angle. Radar data from the 2.5^o elevation are used because this is the lowest elevation at which there is no beam blockage at the gauge sites. As mentioned earlier, since the freezing level was close to the ground (at around 1 km from the mean sea level) for the January 27-28 2021 event, the radar beam at 2.5^o elevation intersected the melting layer bottom at ranges 16 km and beyond from the radar location. A vertical profile correction algorithm was used to project the radar reflectivity contaminated by BB to the ground level according to [40]. The hybrid $R(K_{DP})$ estimators were used for ranges closer to the radar whereas hybrid $R(Z)$ estimators were used for ranges beyond 16 km where the radar beam was contaminated with BB. The freezing

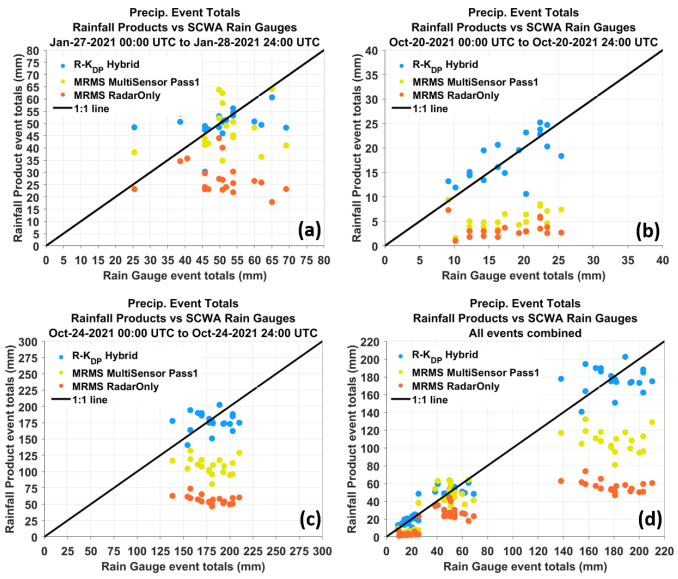

Fig. 15. Scatter plot of event total rainfall accumulations from XSCW radar using hybrid $R(K_{DP})$, MRMS MultiSensor Pass1, and MRMS RadarOnly with all SCWA rain gauges. The black line denotes 1:1 line. (a) January 27-28 2021 event. (b) October 20 2021 event. (c) October 24 2021 event. (d) All events combined.

level during the October 20 and 24 events were about 2.5 km and about 3.5 km from the mean sea level respectively. The 2.5^o radar center beam height at 40 km from the radar location is about is 1.85 km. Therefore, only $R(K_{DP})$ estimators were used for these two events. Rainfall accumulations were calculated using hourly rainfall estimates. Figure 14 show comparisons between X-band radar rainfall estimates, SCWA rain gauge measurements, and the operational MRMS products in terms of cumulative hourly accumulation for the three events at selected SCWA gauge locations. It should be noted that all rain gauges within the radar domain were used in evaluation but only few gauges are shown in the figure for brevity. It can be observed in Figure 14 that the X-Band radar rainfall accumulation matches quite well with the gauge estimates in terms of total rainfall accumulation. The MRMS RadarOnly product which is based on WSR-88D S-Band observations are found to greatly underestimate precipitation relative to the rain gauge values. The MultiSensor Pass 1 product's performance varied from gauge to gauge. It is worth noting that the MultiSensor Pass 1 product at few gauge locations performed better than the X-Band estimates during the January 27-28 2021 event. The reason behind it could be attributed to the fact that the January event has the least amount orographic enhancement among the three events. Given this scenario, the product performs quite well at gauge locations which are probably closely located to the ones used in the inherent gauge correction scheme of the MultiSensor Pass 1 Product. In order to gain more insight into the overall QPE performance the event total accumulations were compared and presented in form of a scatter plot. Figure 15 presents a scatter plot of event total rainfall accumulations between different products versus all rain gauges. A performance metric is presented in Table III in terms to statistical scores of Mean Bias, Mean Absolute Error, and Root Mean Squared Error. Assuming the rain gauge measurements as the ground truth, each score can be defined as following

$$MB = \frac{1}{N}\sum_{n=1}^{N}(R_n - G_n) \tag{17}$$

$$MAE = \frac{1}{N}\sum_{n=1}^{N}(R_n - G_n) \tag{18}$$

$$RMSE = \sqrt{\frac{1}{N}\sum_{n=1}^{N}(R_n - G_n)^2} \tag{19}$$

where G_n and R_n denote the rain gauge and radar rainfall measurement at each rain gauge location respectively. N is the total number of rain gauges. A negative mean bias indicates overall underestimation. It can observed that the hybrid $R(K_{DP})$ has small negative mean bias (not exceeding 3.6 mm) overall indicating very little underestimation compared to the MRMS products. The mean absolute error gives an idea of the magnitude of underestimation or overestimation. When all three events are considered together the overall mean absolute error is less than 9 mm and the root mean squared error is less than 13 mm which is reasonable when compared to the MRMS products. Between the three products, the MRMS RadarOnly has the worst performance in terms of all of the three scores. Overall, the performance of the QPE using the X-Band hybrid $R(K_{DP})$ estimator is the best compared to the MRMS products.

V. Summary and Discussions

Precipitation, in the San Francisco Bay Area, is more often orographically enhanced by the presence of mountains. Previous studies such as [11], [12] have also documented observations of orographic rain in the flat valley regions where orographic induced rainfall is less likely. In this study, two NOAA HMT sites are considered. The MDT site is located in the mountain while the STR site is located in the valley region. DSD characteristics at these two sites were studied and evaluated based on collocated disdrometer and S-PROF observations, reflecting a combination of rainfall processes including bright-band rain with robust ice processes and subsequent melting and non-bright band rain dominated by warm rain collision coalescence below the melting level. Orographic rain, which is referred in this study as NBB rain, is found to have characteristics significantly different than BB rain. It has a higher concentration of smaller drops which are less than 1 mm in diameter. NBB is mainly characterized with lower Z and K_{DP} values when compared to BB rain. Upon comparing the radar parameters with disdrometer rainfall rate, it is observed that NBB rainfall is associated with a higher rainfall rate corresponding to the same Z and K_{DP} values in BB rain. Due to this reason, application of an average radar rainfall relation (derived from DSD data when rainfall types are not distinguished) could lead to substantial underestimation of radar based QPE for periods observing NBB rainfall. Even polarimetric rainfall estimators using average or traditional

coefficients can not provide sufficient accuracy. Given this scenario, there is a need to improve radar based QPE in complex terrain based on methods which can identify NBB rain from BB rain using dual-pol parameters and apply rainfall estimators specific to rainfall types especially NBB rain. To this end, a $Z - Z_{DR}$ threshold is developed in this study which is able to distinguish NBB rain from BB rain and can be applied to radar scan data in real-time. There is some overlap of samples in the $Z - Z_{DR}$ space between the BB and NBB rain which could be mainly due to two reasons. The first is due to the parameterization error which can be improved by more sophisticated techniques such as machine learning based classification. The other possibility for the overlap of samples can be related to the presence of an intermediate rain type known as hybrid rain. This rainfall type is discussed in detail in [9]. Hybrid rainfall is found to have characteristics of both BB and NBB rain. It is suggested that an investigation of the hybrid rainfall type and its inclusion in the algorithm development could yield further improvement in radar based QPE in complex terrains. However, this type of rainfall is not studied separately in this work. The radar rainfall estimators, such as $R(K_{DP})$ and $R(Z)$, are calculated for BB and NBB rain types separately. The coefficients for NBB rainfall estimators are significantly different than the BB rainfall estimators. An average $R(K_{DP})$ relation, considering both BB and NBB rain together, is also developed. It is demonstrated that an average relation results in overestimation in BB periods and significant underestimation in NBB periods. This is one of the main reasons for developing the proposed radar based QPE algorithm in this study. It is well known that K_{DP} possesses significant advantages in radar based rainfall estimation at X-band. Moreover, $R(K_{DP})$ parameterization error is less than that of reflectivity based estimator. However, in case of bright band contamination $R(K_{DP})$ is not suitable. For this reason, $R(Z)$ estimators are also derived for BB and NBB rainfall type and should be used in conjunction with VPR correction in bright band contaminated regions. Other polarimetric estimators such as $R(Z, Z_{DR})$ and $R(Z_{DR}, K_{DP})$ can be developed as well but not discussed in this study. Care should be exercised before application of the polarimetric algorithm on radar data in real time. Since Z_{DR} is an important parameter in the NBB rainfall classification and estimation, it should be well calibrated. Biased Z_{DR} could lead to faulty QPE estimation using the algorithm suggested in this work. This can be considered as a drawback of this algorithm. There are techniques in literature which can be used for Z_{DR} bias correction using PPI data by either observing drizzle at low elevation scans for by observing dry snow at higher elevations. Z_{DR} calibration, using one of these techniques, should be checked frequently. In addition, both Z and Z_{DR} can be calibrated in real time using collocated disdrometer observations. Three rain events with different storm total accumulations from the year 2021 are considered for algorithm evaluation. Application of the algorithm on XSCW radar data demonstrates good performance against the rain gauge estimates. The performance is also contrasted against operational MRMS products such as MultiSensor Pass 1 QPE and RadarOnly QPE. Lower performance metrics of the MRMS products can be accounted for the following reason. Current radar based precipitation identification algorithm used in the MRMS products only aim at differentiating stratiform rainfall from convective rainfall [43]. Orographic rain identification and application of specific rainfall relations is suggested for improving MRMS QPE accuracy in areas of complex terrain. In conclusion, this study suggests a possibility of a more accurate X-band radar based QPE that accounts for changes in rainfall type in the San Francisco Bay Area region.

ACKNOWLEDGMENTS

This research work was supported by the State of California, Sonoma Water, and the NOAA Physical Sciences Laboratory.

REFERENCES

[1] R. Cifelli and V. Chandrasekar, "Dual-polarization radar rainfall estimation," *Washington DC American Geophysical Union Geophysical Monograph Series*, vol. 191, pp. 105–125, 2010.

[2] H. Chen, V. Chandrasekar, and R. Bechini, "An improved dual-polarization radar rainfall algorithm (drops2. 0): Application in nasa ifloods field campaign," *Journal of Hydrometeorology*, vol. 18, no. 4, pp. 917–937, 2017.

[3] G. Skofronick-Jackson, W. A. Petersen, W. Berg, C. Kidd, E. F. Stocker, D. B. Kirschbaum, R. Kakar, S. A. Braun, G. J. Huffman, T. Iguchi *et al.*, "The global precipitation measurement (gpm) mission for science and society," *Bulletin of the American Meteorological Society*, vol. 98, no. 8, pp. 1679–1695, 2017.

[4] S. K. Biswas and V. Chandrasekar, "Cross-validation of observations between the gpm dual-frequency precipitation radar and ground based dual-polarization radars," *Remote Sensing*, vol. 10, no. 11, p. 1773, 2018.

[5] Y. Ma, V. Chandrasekar, and S. K. Biswas, "A bayesian correction approach for improving dual-frequency precipitation radar rainfall rate estimates," *Journal of the Meteorological Society of Japan. Ser. II*, 2020.

[6] J. L. Bytheway, K. M. Mahoney, M. Hughes, and R. Cifelli, "Successes and failures of deterministic precipitation forecasts leading up to the 2017 oroville dam crisis," in *AGU Fall Meeting Abstracts*, vol. 2018, 2018, pp. A11K–2401.

[7] A. B. White, B. J. Moore, D. J. Gottas, and P. J. Neiman, "Winter storm conditions leading to excessive runoff above california's oroville dam during january and february 2017," *Bulletin of the American Meteorological Society*, vol. 100, no. 1, pp. 55–70, 2019.

[8] S. Y. Matrosov, F. M. Ralph, P. J. Neiman, and A. B. White, "Quantitative assessment of operational weather radar rainfall estimates over california's northern sonoma county using hmt-west data," *Journal of Hydrometeorology*, vol. 15, no. 1, pp. 393 – 410, 2014. [Online]. Available: https://journals.ametsoc.org/view/journals/hydr/15/1/jhm-d-13-045_1.xml

[9] A. B. White, P. J. Neiman, F. M. Ralph, D. E. Kingsmill, and P. O. G. Persson, "Coastal orographic rainfall processes observed by radar during the california land-falling jets experiment," *Journal of Hydrometeorology*, vol. 4, no. 2, pp. 264–282, 2003.

[10] B. E. Martner, S. E. Yuter, A. B. White, S. Y. Matrosov, D. E. Kingsmill, and F. M. Ralph, "Raindrop size distributions and rain characteristics in california coastal rainfall for periods with and without a radar bright band," *Journal of Hydrometeorology*, vol. 9, no. 3, pp. 408 – 425, 2008. [Online]. Available: https://journals.ametsoc.org/view/journals/hydr/9/3/2007jhm924_1.xml

[11] S. Y. Matrosov, R. Cifelli, P. J. Neiman, and A. B. White, "Radar rain-rate estimators and their variability due to rainfall type: An assessment based on hydrometeorology testbed data from the southeastern united states," *Journal of Applied Meteorology and Climatology*, vol. 55, no. 6, pp. 1345 – 1358, 2016. [Online]. Available: https://journals.ametsoc.org/view/journals/apme/55/6/jamc-d-15-0284.1.xml

[12] D. E. Kingsmill, P. J. Neiman, and A. B. White, "Microphysics regime impacts on the relationship between orographic rain and orographic forcing in the coastal mountains of northern california," *Journal of Hydrometeorology*, vol. 17, no. 11, pp. 2905–2922, 2016.

[13] J. Marshall, W. Hitschfeld, and K. Gunn, "Advances in weather radar," *Advances in Geophysics*, vol. 2, pp. 1–56, 1955.

[14] D. Rosenfeld, D. B. Wolff, and D. Atlas, "General probability-matched relations between radar reflectivity and rain rate," *Journal of Applied Meteorology and Climatology*, vol. 32, no. 1, pp. 50–72, 1993.

[15] J. Zhang, K. Howard, C. Langston, S. Vasiloff, B. Kaney, A. Arthur, S. Van Cooten, K. Kelleher, D. Kitzmiller, F. Ding *et al.*, "National mosaic and multi-sensor qpe (nmq) system: Description, results, and future plans," *Bulletin of the American Meteorological Society*, vol. 92, no. 10, pp. 1321–1338, 2011.

[16] M. N. Anagnostou, J. Kalogiros, E. N. Anagnostou, M. Tarolli, A. Papadopoulos, and M. Borga, "Performance evaluation of high-resolution rainfall estimation by x-band dual-polarization radar for flash flood applications in mountainous basins," *Journal of hydrology*, vol. 394, no. 1-2, pp. 4–16, 2010.

[17] V. N. Bringi and V. Chandrasekar, *Polarimetric Doppler weather radar: principles and applications*. Cambridge university press, 2001.

[18] S. Lim, D.-R. Lee, R. Cifelli, and S. H. Hwang, "Quantitative precipitation estimation for an x-band dual-polarization radar in the complex mountainous terrain," *KSCE Journal of Civil Engineering*, vol. 18, no. 5, pp. 1548–1553, 2014.

[19] R. Cifelli, V. Chandrasekar, S. Lim, P. C. Kennedy, Y. Wang, and S. A. Rutledge, "A new dual-polarization radar rainfall algorithm: Application in colorado precipitation events," *Journal of Atmospheric and Oceanic Technology*, vol. 28, no. 3, pp. 352–364, 2011.

[20] J. Zhang, K. Howard, C. Langston, B. Kaney, Y. Qi, L. Tang, H. Grams, Y. Wang, S. Cocks, S. Martinaitis *et al.*, "Multi-radar multi-sensor (mrms) quantitative precipitation estimation: Initial operating capabilities," *Bulletin of the American Meteorological Society*, vol. 97, no. 4, pp. 621–638, 2016.

[21] S. E. Yuter and R. A. Houze, "Measurements of raindrop size distributions over the pacific warm pool and implications for z–r relations," *Journal of Applied Meteorology and Climatology*, vol. 36, no. 7, pp. 847–867, 1997.

[22] R. Cifelli, V. Chandrasekar, H. Chen, and L. E. Johnson, "High resolution radar quantitative precipitation estimation in the san francisco bay area: Rainfall monitoring for the urban environment," *Journal of the Meteorological Society of Japan. Ser. II*, vol. 96, pp. 141–155, 2018.

[23] S. K. Biswas, R. Cifelli, and C. Chandra, "Evaluation of quantitative precipitation estimation by s-band radar in complex terrain over the feather river basin in california, usa." in *AGU Fall Meeting Abstracts*, vol. 2018, 2018, pp. A31H–2926.

[24] S. K. Biswas, V. Chandrasekar, R. Cifelli, and J. Bytheway, "Evaluation of the mountain mapper product generated by the multi-radar multi-sensor system (mrms) over the russian river basin region in california," in *98th American Meteorological Society Annual Meeting*. AMS, 2018.

[25] H. Chen, R. Cifelli, V. Chandrasekar, and Y. Ma, "A flexible bayesian approach to bias correction of radar-derived precipitation estimates over complex terrain: Model design and initial verification," *Journal of Hydrometeorology*, vol. 20, no. 12, pp. 2367–2382, 2019.

[26] S. K. Biswas, R. Cifelli, and V. Chandrasekar, "Improving quantitative precipitation estimation by x-band dual-polarization radars in complex terrain over the bay area in california, usa," in *IGARSS 2020-2020 IEEE International Geoscience and Remote Sensing Symposium*. IEEE, 2020, pp. 5411–5414.

[27] J. L. Bytheway, M. Hughes, K. Mahoney, and R. Cifelli, "On the uncertainty of high-resolution hourly quantitative precipitation estimates in california," *Journal of Hydrometeorology*, vol. 21, no. 5, pp. 865–879, 2020.

[28] L. E. Johnson, R. Cifelli, and A. White, "Benefits of an advanced quantitative precipitation information system," *Journal of flood risk management*, vol. 13, p. e12573, 2020.

[29] P. Waterman, "Matrix formulation of electromagnetic scattering," *Proceedings of the IEEE*, vol. 53, no. 8, pp. 805–812, 1965.

[30] A. Tokay, D. B. Wolff, and W. A. Petersen, "Evaluation of the new version of the laser-optical disdrometer, ott parsivel2," *Journal of Atmospheric and Oceanic Technology*, vol. 31, no. 6, pp. 1276–1288, 2014.

[31] D. Jash, E. Resmi, C. Unnikrishnan, R. Sumesh, T. Sreekanth, N. Sukumar, and K. Ramachandran, "Variation in rain drop size distribution and rain integral parameters during southwest monsoon over a tropical station: An inter-comparison of disdrometer and micro rain radar," *Atmospheric Research*, vol. 217, pp. 24–36, 2019.

[32] D. Atlas, R. Srivastava, and R. S. Sekhon, "Doppler radar characteristics of precipitation at vertical incidence," *Reviews of Geophysics*, vol. 11, no. 1, pp. 1–35, 1973.

[33] J. Testud, E. Le Bouar, E. Obligis, and M. Ali-Mehenni, "The rain profiling algorithm applied to polarimetric weather radar," *Journal of Atmospheric and Oceanic Technology*, vol. 17, no. 3, pp. 332–356, 2000.

[34] M. Thurai, W. Petersen, A. Tokay, C. Schultz, and P. Gatlin, "Drop size distribution comparisons between parsivel and 2-d video disdrometers," *Advances in Geosciences*, vol. 30, pp. 3–9, 2011.

[35] B. K. Seela, J. Janapati, P.-L. Lin, K. K. Reddy, R. Shirooka, and P. K. Wang, "A comparison study of summer season raindrop size distribution between palau and taiwan, two islands in western pacific," *Journal of Geophysical Research: Atmospheres*, vol. 122, no. 21, pp. 11–787, 2017.

[36] E. A. Brandes, G. Zhang, and J. Vivekanandan, "An evaluation of a drop distribution–based polarimetric radar rainfall estimator," *Journal of Applied Meteorology*, vol. 42, no. 5, pp. 652–660, 2003.

[37] M. Thurai, P. Gatlin, and V. Bringi, "Separating stratiform and convective rain types based on the drop size distribution characteristics using 2d video disdrometer data," *Atmospheric Research*, vol. 169, pp. 416–423, 2016.

[38] S. Y. Matrosov, K. A. Clark, and D. E. Kingsmill, "A polarimetric radar approach to identify rain, melting-layer, and snow regions for applying corrections to vertical profiles of reflectivity," *Journal of applied meteorology and climatology*, vol. 46, no. 2, pp. 154–166, 2007.

[39] R. Sánchez-Diezma, I. Zawadzki, and D. Sempere-Torres, "Identification of the bright band through the analysis of volumetric radar data," *Journal of Geophysical Research: Atmospheres*, vol. 105, no. D2, pp. 2225–2236, 2000.

[40] Y. Qi, J. Zhang, P. Zhang, and Q. Cao, "Vpr correction of bright band effects in radar qpes using polarimetric radar observations," *Journal of Geophysical Research: Atmospheres*, vol. 118, no. 9, pp. 3627–3633, 2013.

[41] E. A. Brandes, G. Zhang, and J. Vivekanandan, "Corrigendum," *J. Appl. Meteor.*, vol. 44, p. 186, 2005.

[42] S. M. Martinaitis, S. B. Cocks, M. J. Simpson, A. P. Osborne, S. S. Harkema, H. M. Grams, J. Zhang, and K. W. Howard, "Advancements and characteristics of gauge ingest and quality control within the multi-radar multi-sensor system," *Journal of Hydrometeorology*, vol. 22, no. 9, pp. 2455–2474, 2021.

[43] Y. Qi, J. Zhang, and P. Zhang, "A real-time automated convective and stratiform precipitation segregation algorithm in native radar coordinates," *Quarterly Journal of the Royal Meteorological Society*, vol. 139, no. 677, pp. 2233–2240, 2013.